https://doi.org/10.32604/zkg.2026.078624

ARTICLE

Performances and microstructures of different cementitious materials during simulated biological sulfuric acid erosion

Jin Yang[1,2,3], Xudong Zhao[2], Xingyang He[1,2,*], Gaoyuan Zhai[2], Ying Su[1,2], Yingbin Wang[1,2], Yubo Li[1,2] and Bohumír Strnadel[3]

[1]China-Ethiopia Belt and Road Joint Laboratory on Civil Engineering Green Construction, Intelligent Operation and Maintenance, Hubei University of Technology, Wuhan, China
[2]School of Civil Engineering, Architecture and Environment, Hubei University of Technology, Wuhan, China
[3]Centre for Advanced Innovation Technologies, VSB-Technical University of Ostrava, Ostrava-Poruba, Czech Republic
*Corresponding Author: Xingyang He. Email: hexycn@163.com

Received: 05 January 2026; Accepted: 17 March 2026

ABSTRACT: Bioacidic erosion from microbial activity threatens concrete infrastructure in sewage systems. This study evaluated the durability of four cementitious materials under simulated bioacid attack for 120 days. Results indicated that Ultra-High Performance Concrete (UHPC) exhibited superior resistance, with mass loss of 0.17% and compressive strength loss of 7.54%, representing reductions of 95.15% and 72.07% compared to Ordinary Portland Cement (OPC), respectively. Microstructural analysis revealed that UHPC's dense matrix (total porosity of 8.6% versus 23.86–34.13% for other materials) and ettringite formation contributed to its enhanced stability. In contrast, Alkali-Activated Slag (AAS) and Calcium Sulfoaluminate Cement (CSA) exhibited cracks and voids, indicating poor durability. The corrosion mechanisms varied among materials: UHPC resisted sulfate attack through its dense microstructure; CSA suffered from ettringite instability; AAS degraded via calcium aluminate hydrate decomposition; and OPC showed severe structural deterioration. These findings demonstrate that UHPC possesses significant potential as a high-performance protective material for sewage infrastructure applications.

KEYWORDS: Sewage disposal; acid-resistant; deterioration mechanisms; erosion products

1 Introduction

With the accelerating trend of global urbanization, the discharge of domestic sewage has exhibited exponential growth, thereby posing an unprecedented dual threat to both the ecological environment and public health. In this context, advanced sewage purification technology has gradually emerged as the key to overcoming the current challenges. Concurrently, the construction scale of sewage collection and treatment facilities has been continuously expanding, with the construction of sewage pipe networks and treatment plants being propelled to the forefront of urban infrastructure development. By 2024, U.S. cities had established a vast sewage system comprising approximately 16,000 wastewater treatment plants and 800,000 miles of sewers [1, 2]. European countries have approximately 50,000 sewage treatment plants and a combined drainage system length of nearly 700,000 km [3]. Cement concrete materials are extensively utilized in the construction of sewage infrastructure, attributed to their exceptional mechanical properties, high moldability, and relatively moderate costs [4]. Nevertheless, within the specialized context of sewage environments, microbial activity progressively supersedes conventional physical and chemical factors as the primary contributor to concrete structural degradation [5]. Microbially induced concrete corrosion has emerged as a rampant issue, entailing substantial economic losses and posing significant public safety hazard [6–8]. For instance, in Belgium's Flanders region, the estimated cost of sewer maintenance indicates that biocorrosion alone can incur expenses of up to 5 million euros annually. In the United States, repairing or replacing deteriorated sewer infrastructure costs over $3 billion annually, affecting up to 4600 miles of pipelines [9]. Similarly, Australia estimates annual losses of AUD 250 million due to water and wastewater transport network failures [10]. Furthermore, the biodegradation of concrete significantly diminishes the service life of concrete-based wastewater treatment facilities, potentially shortening it to 30–50 years [11].

In response to this global challenge, extensive research has been conducted to elucidate the corrosion mechanisms of microbially induced concrete degradation. Studies have demonstrated that

MATERIALS

the deterioration of concrete in sewage systems is ultimately the result of a complex chain of chemical and biochemical reactions. In the early stages of sewage exposure, heterotrophic bacteria and fungi initially proliferated on the surfaces of sewer walls and settling layers where organic matter accumulates. Through anaerobic respiration, organic matter is metabolized into carbon dioxide and weak acids. Concurrently, Sulfate-Reducing Bacteria (SRB) reduce sulfate ions present in sewage to gaseous Hydrogen Sulfide (H_2S) within anaerobic microenvironments. Once hydrogen sulfide is released into the sewer space, it penetrates concrete pores via gas-phase diffusion and dissolution. In concrete prepared with OPC, the pore solution exhibits a pH value as high as 13.5, indicative of its strongly alkaline nature [12]. This highly alkaline environment initiates chemical acid-base neutralization reactions, with hydrogen sulfide acidification reactions primarily driving a gradual local pH decrease. When the pH decreases to approximately 9.5, Neutral Sulfur-Oxidizing Bacteria (NSOB) begin to colonize the concrete surface. Under oxygen-rich conditions, these bacteria thoroughly oxidize sulfides to Sulfuric Acid (H_2SO4), generating intermediate products such as elemental sulfur, polysulfides, and thiosulfates [13]. As biosulfuric acid production increases, Acidophilic Sulfur-Oxidizing Bacteria (ASOB) can proliferate in acidic environments (pH ≤ 4). Like NSOB, ASOB continuously produces biosulfuric acid during aerobic respiration, which is recognized as a primary contributor to concrete structural deterioration [14–16]. Over time, acidic substances infiltrate and erode the concrete matrix, inducing the dissolution of hydrated cement compounds (e.g., calcium hydroxide CH, hydrated calcium silicate C-S-H) and facilitating the formation of sulfate minerals, including gypsum and ettringite. This leads to a substantial crystallization pressure within the concrete, ultimately compromising its structural integrity [17–19].

Microbially induced concrete corrosion involves coupled chemical and biochemical reactions. Bacteria, fungi, and their metabolites synergistically accelerate the degradation of concrete structures. Concrete corrosion caused by biological sulfuric acid has become a key focus in current materials science research. Currently, microbial erosion testing methods for concrete materials are categorized into on-site *in-situ* testing and laboratory simulation experiment [20, 21]. Field *in-situ* experiments are constrained by the complex variables of natural sewer environments, prolonged reaction cycles, and high reproducibility challenges [22]. In contrast, laboratory simulation experiments, which precisely apply sulfuric acid (from biological or chemical sources, or both), provide a controlled approach to elucidate the corrosion mechanisms of concrete induced by microorganisms in natural environments, with results exhibiting high applicability [23–25]. However, bacterial cultivation methods are limited by a prolonged acid production cycle [26]. Nevertheless, simulated biological corrosion of concrete matrix using sulfuric acid in laboratory settings has been widely accepted by the academic community [27–29]. In this study, sulfuric acid served as the simulated acid source.

Currently, numerous researchers are investigating the acid durability, mechanical properties, pore structure evolution, and surface corrosion characteristics of various cementitious materials under simulated biological acid attack. These cutting-edge research findings provide a robust foundation for enhancing the service life and reliability of cementitious materials in aggressive environments. Thiobacillus metabolic activity and the acid source are inhibited and neutralized by aluminate cement, thereby establishing a robust defense against bio-acid erosion, as confirmed by Ding et al. [30]. In their *in-situ* sewer experiments, Bakera and Alexander [31] demonstrated that CSA exhibits superior acid resistance compared to sulfate-resistant Portland cement. This superiority is attributed to its primary hydration products, ettringite and Aluminum Hydroxide (AH_3), which possess exceptional acid resistance. The OPC/CSA composite cementitious system also demonstrates significant potential to enhance the cement matrix's resistance to sulfuric acid corrosion. The formation of a dense protective layer through pore-filling with C-(A)-S-H gel in AAS was highlighted by Lee and Lee [32], which contributes to its superior resistance to water and acid. Presently, research on cementitious material corrosion in simulated biological acid environments remains relatively limited. Most existing studies focus on traditional Portland cement concrete, composite cement concrete, and gypsum-based cement concrete, with limited attention to UHPC [33–36]. Furthermore, comparative studies across different cementitious materials under simulated biological acid conditions are nearly non-existen [37]. Consequently, systematic analyses of durability and microstructural responses of various cementitious materials under acid erosion are essential for informed material selection and optimal wastewater treatment facility design.

This study investigates four cementitious materials of UHPC, AAS, CSA, and OPC to evaluate their durability and track microstructural evolution under simulated acid solution erosion. Through precise control of immersion time (30, 60, 90, and 120 days), the study comprehensively assesses concrete durability attenuation via appearance characterization, mass loss quantification, and erosion coefficient calculations. Additionally, a thorough investigation into the concrete degradation mechanisms is performed using advanced characterization methods such as Thermogravimetric Analysis (TGA), Scanning Electron Microscopy (SEM), Mercury Intrusion Porosimetry (MIP), and X-Ray Diffraction (XRD) analysis. This study aims to address the research gap in cementitious

materials subjected to biological acid erosion and offers theoretical insights and practical guidance for the long-term operation and maintenance of wastewater treatment facilities.

2 Materials and methods

2.1 Raw materials

The raw materials used in this experiment included OPC, CSA, GGBS, and UHPC. Ordinary Portland cement (P·O 42.5) was sourced from Hubei Huaxin Cement Co. Rapid-setting sulfur-aluminate cement (R·SAC 42.5) was obtained from Jiangxi Golden Eagle Building Materials Co. The UHPC commercial masterbatch used in this study was also procured from Hubei Huaxin Cement Co., Ltd., China. The oxide compositions of OPC, CSA, GGBS and UHPC are shown in Table 1. The simulated acid solution was prepared using 98% concentrated sulfuric acid, a chemical reagent with a mass fraction produced by Sinopharm Chemical Reagent Co., Ltd. The sodium hydroxide used is a white solid powder. The water glass utilized in this study was a pale yellow liquid, with a modulus of 3.3 and a solid content of 40%. The high-range water reducer employed in the experiment was a high-efficiency polycarboxylic acid powder PCE superplasticizer.

2.2 Proportioning and sample preparation

In the experimental design for simulated bio-acid attack, four cementitious systems were investigated: OPC, CSA, AAS, UHPC. The detailed mix proportions of the mortars used are presented in Table 2. The mortar specimens were prepared as 40 mm × 40 mm × 40 mm cubes by pouring the mixtures into molds and compacting them on a vibrating table. Following demolding, the mortar cubes were cured in a standard curing room for 28 days.

After 28 days of curing were submerged in a simulated acid solution with a pH of 2. Each sample was positioned with a minimum spacing of 3 cm to ensure uniform exposure, and spacers were placed underneath them. Additionally, the solution was replaced every two weeks to maintain a stable pH throughout the immersion period. Changes in the surface appearance and mass of each type of mortar sample were recorded after 30, 60, 90, and 120 days of immersion.

2.3 Test methods

2.3.1 Mass loss rate

Upon reaching the soaking cycle, the mortar specimen is subjected to drying in a constant-temperature oven maintained at 30°C for a duration of 6 h. Subsequently, the mass of the specimen is accurately measured utilizing a high-precision electronic scale, which possesses a precision level of 0.01 g. The mass loss rate of the mortar specimens, ΔM, was calculated using the formula:

$$\Delta M = \frac{M(g) - M_n(g)}{M(g)} \times 100\% \quad (1)$$

where: ΔM is the mass loss rate of mortar after periodic immersion, %; M_n is the mass of mortar specimen after periodic immersion, g; M is the initial mass of mortar specimen before immersion, g.

2.3.2 Coefficient of erosion

When the mortar specimens reached the age of immersion, they were removed and placed at room temperature to dry. The compressive strength test was carried out using DYE-300A compressive testing machine, the loading speed of the press was 2.4 kN/s. The average value of 3 valid specimens was taken as the final compressive strength.

Table 1 **Chemical composition of OPC, CSA, GGBS and UHPC**

Sample	CaO	SiO_2	Al_2O_3	Fe_2O_3	MgO	Na_2O	MnO	P_2O_5	SO_3	LOI[a]
OPC	65.1	21.1	4.1	3.1	1.53	0.08	0.19	0.25	1.26	2.28
CSA	42.25	6.86	36.46	2.28	1.33	0.22	–	–	8.82	0.67
GGBS	36.52	38.35	10.88	0.52	8.77	0.49	1.25	–	–	0.26
UHPC	58.22	25.03	6.36	3.18	2.39	0.448	0.128	0.980	2.29	2.4

Note: LOI[a] is the amount of loss on ignition at 1000°C; GGBS is used only as a raw material for AAS, not as an independent testing group.

Table 2 **Baseline mix ratios for mortars prepared with various cementitious materials**

Sample	W/B (ratio)	B/S (ratio)	PCE (%)	NaOH (%)	Na_2SiO_3 (%)
OPC	0.4	1:2	–	–	–
UHPC	0.175	1:1.1	8	–	–
CSA	0.4	1:2	–	–	–
AAS	0.4	1:2	–	3	15

Note: W/B is water-binder ratio, B/S is binder-aggregate ratio; Sodium hydroxide, sodium silicate is based on mass of the binder (GGBS).

The erosion coefficient K of the mortar specimen was calculated by the formula:

$$K = \frac{F_s}{F_w} \times 100\% \quad (2)$$

where: K is the erosion coefficient; F_s is the compressive strength of mortar specimens after the specified age of acid immersion in MPa; and F_w is the compressive strength of specimens in the control group of the clear-water experiments under the same immersion period in MPa.

2.3.3 X-Ray diffraction

The samples were soaked in ethanol, oven dried at 50°C for 24 h, ground into powder and sieved through a 75 µm screen. A D8-Advance X-ray diffractometer was used to test the surface samples of selected soaked specimens. The goniometer radius was set at more than 200 mm, with a scanning range of 5° to 80° and a scanning speed of 10°/min.

2.3.4 Thermal analysis

Thermogravimetric analysis was carried out using STA449F3 thermogravimetric analyzer. About 50 mg of powder samples were selected for testing, nitrogen was used as the protective gas, and the test temperature range was 40–1000°C with a temperature increase rate of 10°C/min.

2.3.5 Fourier transform infrared spectral analysis

Fourier Transform Infrared Spectroscopy (FTIR) was used for analysis. The dried specimen surface samples were ground and mixed with potassium bromide in the ratio of 1:100 for tableting. The wavelength range of the test was 4000 cm^{-1}–400 cm^{-1}; the minimum precision was 1 cm^{-1}, and the sample and potassium bromide were weighed by a scale with an absolute precision of 0.1 mg. The room temperature was maintained at 20 ± 2°C and the relative humidity was less than 50%.

2.3.6 Mercury intrusion porosimetry

Flake samples at a location of 5 mm from the surface of the mortar specimens were selected for drying, after which the samples were cut to a size of 1.0–1.5 cm. Mercury Intrusion Porosimetry of the corroded mortar specimens was carried out using a Poremaster-60 pore gauge. The low-pressure test range of the pore structure analyzer was set to 0~40 Psia, and the high-pressure test range was set to 0~60,000 Psia; the contact angle was set to 140°.

2.3.7 Scanning electron microscope-energy dispersive spectrometer

A scanning electron microscope (FE-SEM, QUANTA FEG 450) was used to observe the microscopic morphology. Before testing, the samples were bonded with conductive adhesive on the surface, fixed on the sample base and sprayed with gold under vacuum environment. During the analysis of the morphology of the corrosion layer, the mortar corrosion layer specimens were face swept using an Energy Dispersive Spectrometer (EDS). The EDS was operated by a Link-Isis (Oxford Instruments) X-ray energy dispersive detector for chemical compositional analysis.

3 Results and discussion

3.1 Visual appearance

Surface morphology serves as a critical parameter for assessing the progression of acid corrosion, providing direct visual evidence of corrosion product formation and surface degradation patterns. The appearance of four mortar specimens immersed in a simulated acid solution changed over a period of 0 to 120 days, as illustrated in Figure 1. The mortar specimens subjected to acid attack exhibited deterioration, with white corrosion products forming on their surfaces. This phenomenon indicates the formation of gypsum, a product of the acid attack process [38–40]. Following 120 days of exposure to simulated acidic conditions, the UHPC specimens exhibited minimal surface deterioration while retaining their structural integrity. The specimens demonstrated no observable surface spalling and remained crack-free throughout the testing period. Following 90 days of acid exposure, OPC specimens exhibited a marked increase in surface roughness, attributable to the progressive detachment of corrosion-induced particulate matter. Extended exposure to acidic conditions (120 days) resulted in substantial surface deterioration, with pronounced cracking and pore formation evident in both AAS and CSA cement specimens. This phenomenon can be attributed to the formation of gypsum as an expansive byproduct, which increases the solid volume and consequently generates elevated internal pressure [41]. The UHPC mortar specimens demonstrated superior surface integrity and morphological stability under acidic conditions compared to specimens from the three alternative cementitious systems. This performance disparity stems from the superior densification characteristics of the UHPC matrix, which significantly impedes sulfate ion migration by minimizing transport pathways [42].

3.2 Mass loss rate

This study systematically investigated the acid resistance of four cementitious systems to evaluate their long-term durability under aggressive chemical exposure. The mass changes of four mortar samples exposed to simulated acid solution for 0–120 days are shown in Figure 2a, where mass loss is denoted by negative values, indicating an increase in mass. During the initial immersion period, all four cementitious systems exhibited measurable mass gain when exposed to the simulated acidic environment. The observed mass increase likely results from two concurrent mechanisms: (1) acidic decomposition of

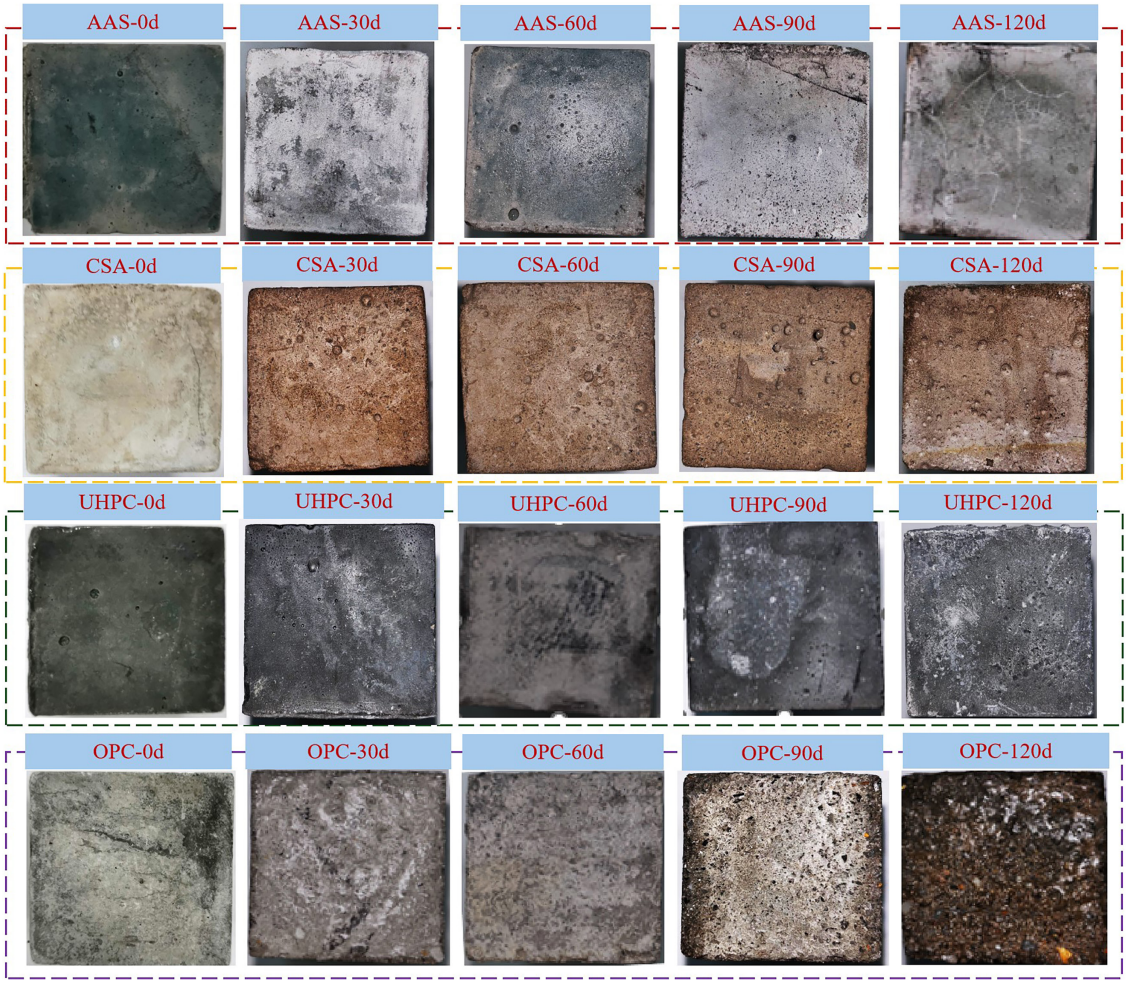

Figure 1 Appearance morphology of different types of mortar specimens after 120 days of simulated acid erosion

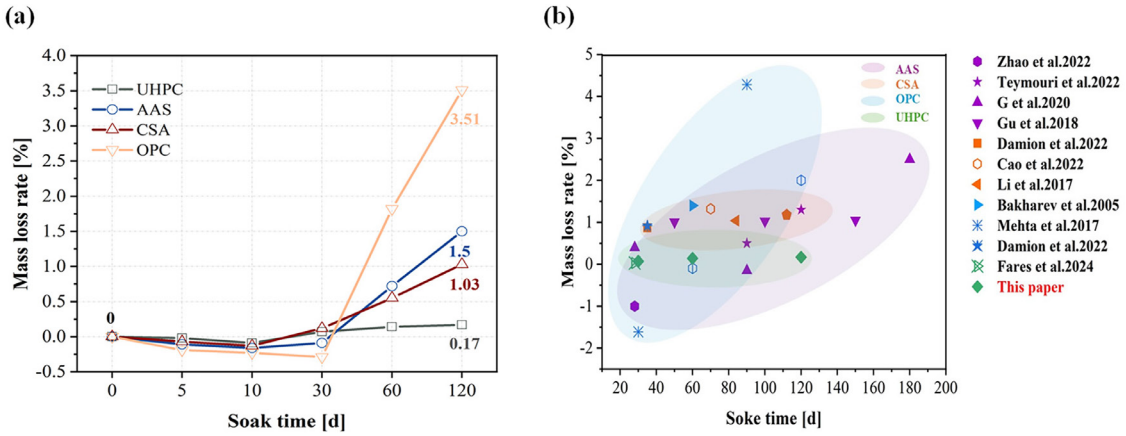

Figure 2 (a) Mass variation of mortar specimens following 120 days of simulated acid erosion; (b) Comparative analysis of quality loss in different studies

Calcium Hydroxide ($Ca(OH)_2$) hydration products by hydrogen ions (H^+), and (2) subsequent precipitation of gypsum ($CaSO_4 \cdot 2H_2O$) through reaction between liberated calcium ions (Ca^{2+}) and sulfate ions (SO_4^{2-}) at the specimen surface or within pore structures. This secondary phase formation contributes to net mass gain due to gypsum's low solubility. Furthermore, ongoing cement hydration contributes significantly to the observed mass gain, as continued formation of hydration products increases the solid phase volume within the cementitious matrix [43]. Following 120 days of immersion in a simulated sulfuric acid solution, the measured mass loss rates followed the order: UHPC (0.17%) < CSA (1.03%) < AAS (1.5%) < OPC (3.51%). Notably, the UHPC specimens exhibited

superior acid resistance, as evidenced by their significantly lower mass loss compared to other cementitious systems. This enhanced performance can be attributed to the optimized particle packing in UHPC, where the fine aggregates effectively reduce porosity through a dense microstructural arrangement, thereby limiting acid penetration pathways. Concurrently, a pozzolanic reaction between supplementary cementitious materials and calcium hydroxide ($Ca(OH)_2$) generated additional C-S-H gel, thereby reducing overall porosity and enhancing microstructural density [44]. Consequently, following exposure to high sulfate concentrations, the UHPC matrix maintains minimal mass loss, demonstrating exceptional chemical stability in aggressive sulfate environments.

Compared to Figure 2a, 2b illustrates the mass changes of four mortar samples subjected to sulfuric acid erosion across various studies. The significant variance in literature data stems from variations in experimental conditions, such as acid type and concentration, differences in materials' composition and origin, and disparities in testing methodologies. These factors collectively influence the mass loss rate and erosion coefficient of the materials. Analysis of the data reveals the following ranges of mass change for the different mortar types under study: for AAS, the range is from –0.09% to 2.5% [45–48]; for CSA, from 0.12% to 1.32% [49–52]; for OPC, from –1.61% to 4.28% [50, 53–55]; and for UHPC, the range is relatively narrow, from 0.03% to 0.17% [56]. UHPC exhibited the lowest mass loss across all studies, thereby further validating its superior durability in acid-aggressive environments. This finding indicates that UHPC possesses better corrosion resistance and the lowest mass loss rate compared to other materials in sulfuric acid environments.

3.3 Coefficient of erosion

Based on prior research, variations in the compressive strength of mortar cubes serve as a reliable indicator of their acid resistance [57]. This deterioration is attributed to a process called "softening" process. The acid attack progressively degrades the surface layer of the mortar specimen, consequently diminishing its load-bearing capacity and compressive strength. This "softening" process is facilitated by the formation of gypsum erosion products on the surface of the cube [58]. At this stage, the mass of all mortar specimens continued to increase. This was attributed to the ongoing diffusion of SO_4^{2-} from the acidic solution into the interior of the mortar, which further triggered the sulfate erosion reaction. The change of erosion coefficient of mortar samples immersed in simulated acid solution for 120 days is depicted in Figure 3a. As indicated by the results presented in the figure, the mortar specimens subjected to acid erosion exhibited varying degrees of deterioration. As the acid immersion duration increased, the specimens exhibited progressive reduction in compressive strength. The accelerated decline in erosion coefficient directly correlates with deteriorating load-bearing capacity, demonstrating the cumulative damaging effects of acid attack on mechanical properties. Further analysis indicates that the erosion coefficient decreases significantly over time, suggesting that the acid resistance of the material deteriorates progressively with increasing immersion duration. Following 120 days of acid exposure, the specimens exhibited significant reductions in erosion resistance, with residual coefficients of: UHPC (92.46%), AAS (83.63%), CSA (87.63%), and OPC (72.69%)—representing decreases of 7.54%, 16.37%, 12.37%, and 27.31% from their initial values, respectively. These results demonstrate a significant variation in the acid resistance properties among the different material systems. Specifically, UHPC exhibited the best acid resistance, while OPC showed relatively poor acid resistance. This finding is consistent with the observed changes in appearance and mass loss of the mortar samples. The enhanced acid resistance of UHPC primarily stems from its incorporation of silica fume (SF) and fly ash (FA). These supplementary cementitious materials

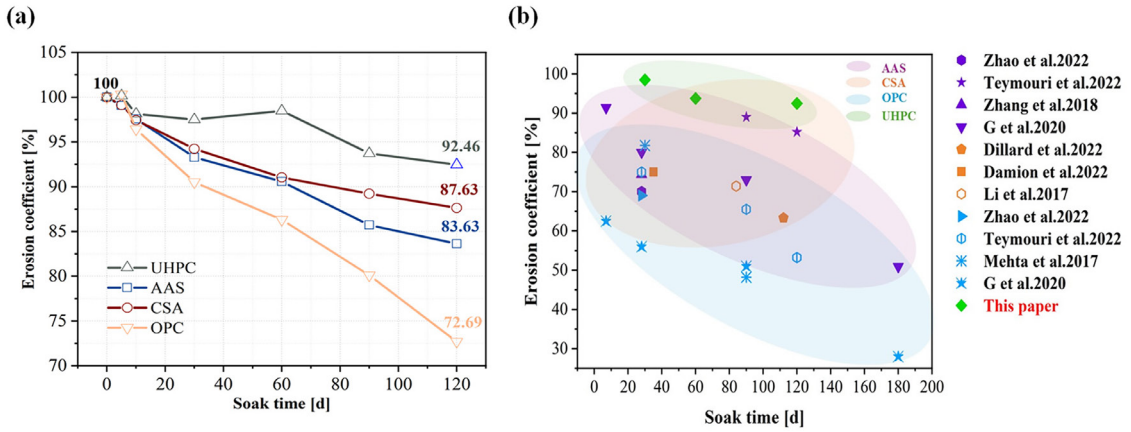

Figure 3 (a) Erosion coefficient changes of various mortar specimens after 120 days of simulated acid erosion; (b) Comparative analysis of compressive strength across different studies

participate in pozzolanic reactions, generating additional C–S–H gel that significantly improves microstructural densification and reduces permeability. However, as acid erosion progresses further, the C–S–H gel is consumed in large quantities. This leads to the internal softening of the cementitious matrix and a reduction in the bonding force, thereby resulting in a decrease in mortar strength. Both the CSA and AAS systems exhibited superior initial acid resistance compared to conventional OPC. In the CSA system, the primary hydration products—AFt and AH_3 possess relatively low chemical reactivity in acidic environments, attributed to their stable crystalline structures. This inherent stability enhances the material's durability during early-stage acid exposure. The CSA system undergoes hydration without forming portlandite ($Ca(OH)_2$), and its predominant hydration products exhibit lower chemical reactivity with acidic solutions compared to conventional cement phases. This distinctive chemistry confers superior initial acid resistance during the early stages of immersion. However, under prolonged acid exposure, AFt in the CSA mortar undergoes progressive transformation to $CaSO_4{\cdot}2H_2O$. This phase transition induces crystallization pressure within the matrix, generating internal stresses that ultimately compromise the material's structural integrity and mechanical strength [59]. The AAS material system contains a high concentration of alkaline ions, which is attributed to the introduction of strong alkaline activators. These ions can partially neutralize the acidity of the solution, thereby retarding the corrosion process. Slag, characterized by its high vitreous silica-alumina content, exhibits strong early-stage reactivity when activated by alkaline solutions. While this promotes rapid formation of hydration products, the resulting chemical shrinkage and self-desiccation often induce microstructural stresses that manifest as late-stage shrinkage cracking in the hardened matrix. Microcracks facilitate the diffusion of SO_4^{2-}, thereby exacerbating the transformation of AFt and increasing the risk of swelling and cracking [45]. "During advanced stages of acid exposure, the AAS system exhibited marked deterioration, as evidenced by a substantial reduction in erosion resistance. This accelerated degradation suggests depletion of the material's alkaline buffering capacity and progressive breakdown of its aluminosilicate network under sustained acidic conditions. For OPC materials, the acid reacts with $Ca(OH)_2$ in the cement hydration products to form insoluble $CaSO_4$. This reaction consumes the cement's alkaline reserves, progressively reducing the pH of the pore solution and destabilizing the C–S–H gel framework. The resulting loss of alkalinity accelerates matrix dissolution and compromises the structural integrity of the cementitious system. Calcium sulfate may be further converted to $CaSO_4{\cdot}2H_2O$, commonly known as gypsum, under the continuous influence of acid. This phase transformation is accompanied by significant volume expansion, which induces increased internal stress within the cement matrix. These stresses can lead to the formation of cracks and pores, thereby reducing the material's compactness and mechanical properties. Additionally, the interaction of acid with C–S–H can result in the substitution of Ca^{2+} ions by SO_4^{2-} ions, forming soluble compounds. This process disrupts the gel structure of C–S–H, thereby weakening the bonding within the cement matrix. These structural alterations diminish the effective load-bearing area of the material, thereby further reducing its compressive strength.

The compressive strength of mortar samples in different studies, as shown in Figure 3b, was further evaluated to assess the durability of the material [45–47, 49, 50, 52, 60]. The data analysis clearly demonstrates that UHPC consistently achieves superior compressive strength across all studies, significantly outperforming conventional cementitious materials. In contrast, OPC consistently demonstrated the lowest compressive strength across all studies, with a pronounced decreasing trend over time [45–47, 55]. The analytical results demonstrate that UHPC maintains superior durability in sulfuric acid environments, preserving over 90% of its compressive strength after prolonged exposure. In contrast, OPC shows marked susceptibility to acid attack, exhibiting severe strength degradation (approximately 30% loss) under identical conditions. This performance differential highlights UHPC's enhanced resistance to chemical deterioration mechanisms. This finding underscores the superior performance of UHPC when subjected to sulfuric acid attack, while OPC exhibits more rapid deterioration in long-term acidic environments.

3.4 X-Ray diffraction analysis

To identify the corrosion products, samples exposed to a simulated acid environment for 120 days were analyzed using X-ray diffraction (XRD). As illustrated in Figure 4, the XRD patterns of UHPC, AAS, CSA, and OPC mortar samples were analyzed. The results indicate that the primary crystalline phases within the corrosion layer are gypsum, calcite, and calcium hydroxide. $CaSO_4{\cdot}2H_2O$ formed within the matrix as a result of SO_4^{2-} ion penetration. Additionally, weak $CaCO_3$ diffraction peaks were detected in the XRD pattern, suggesting that the hydration products of the specimen underwent carbonation due to exposure to atmospheric CO_2 [61]. Furthermore, the XRD patterns exhibited notable variations across the different material systems. Studies have demonstrated that ultra-high-performance concrete (UHPC) mortar possesses exceptional acid resistance, attributable to its dense microstructure and minimal porosity [62]. The detection of $CaSO_4{\cdot}2H_2O$ diffraction peaks confirms the ongoing reaction of SO_4^{2-} with CH and C-S-H gels. The resulting gypsum crystals exhibit a

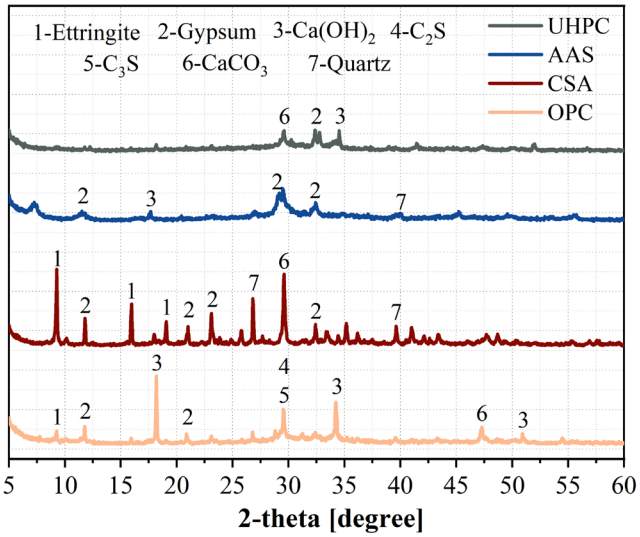

Figure 4 XRD patterns of UHPC, AAS, CSA and OPC acid etching layers

dense distribution along aggregate interface. In the UHPC system, SF reacts with CH—a cement hydration product—to form additional C-S-H. This secondary C-S-H phase enhances the interfacial bond between quartz sand particles and unhydrated cement, while simultaneously increasing the elastic modulus of the specimen's surface layer. Furthermore, this reaction contributes to improved impermeability characteristics of the composite material. However, during acid exposure, the co-precipitation and growth of gypsum crystals generate expansive stress within the matrix, ultimately inducing microcrack formation. In the AAS system, XRD analysis revealed that the corrosion layer consisted primarily of $CaSO_4 \cdot 2H_2O$, with no detectable calcium aluminate ferrite monosulfate phases. Given that slag primarily consists of calcium and silicon (approximately 75%) and has a low aluminum content, the formation of calcium- and aluminum-rich AFt products is limited. Consequently, the primary corrosion product in the AAS system is gypsum. The hydration product of AAS is a C-A-S-H gel with a low Ca/Si ratio. The presence of gypsum indicates that SO_4^{2-} has diffused into the alkali-activated material, leading to the dissociation and decalcification of the calcium-based gel. This observation is consistent with the gypsum diffraction peak at 28.1°. Studies have demonstrated that sulfate attack in alkali-activated materials is fundamentally governed by alkaline component leaching. The coupled processes of SO_4^{2-} diffusion and alkali ion leaching synergistically accelerate gel decalcification, while concurrently promoting pore structure degradation in alkali-activated materials under acidic conditions [46]. In the XRD pattern of CSA mortar, the primary detected diffraction peaks correspond to gypsum and calcite. During the early stages of CSA hydration, the main hydration products AFt and aluminum AH_3. The presence of AH_3 serves as an acid-resistant barrier, thereby retarding further corrosio [63]. With the continuous penetration of SO_4^{2-}, the AFm phase is converted to the AFt phase. The accumulation of AFt eventually leads to matrix swelling and cracking. The XRD patterns of OPC mortar exhibit relatively complex changes, likely due to the reaction of silicate minerals in the cement with sulfuric acid, resulting in the formation of new compounds.

3.5 Thermogravimetric analysis

To elucidate the degradation mechanisms during acid attack, TGA was conducted. As illustrated by the differential thermogravimetric (DTG) curves in Figure 5a, the influence of sulfate attack on the weight loss peak of the hydration product (CH) in UHPC, AAS, and OPC materials is relatively minor. The differential DTG curves demonstrated that sulfate exposure had minimal impact on the dehydration peaks of CH in UHPC, AAS, and OPC systems, suggesting relatively stable hydration products under these conditions. Between 50°C and 200°C, the weight loss peaks showed overlapping of multiple phases, mainly including gypsum, C-S-H gels, and AFt phases [64]. The investigation into the mass loss characteristics of the four types of cementitious materials, as shown in Figure 5b, revealed significant differences. In the low-temperature range (100–150°C), mass losses followed the order: CSA (6.92%) > OPC (3.51%) > AAS (3.09%) > UHPC (2.32%). Conversely, in the high-temperature range (400–500°C), the trend was reversed with OPC exhibiting the highest mass loss (3.24%), followed by AAS (1.72%), UHPC (1.03%), and CSA (0.88%). The weight loss peak in the CSA system is more pronounced than in other systems, which is closely related to its material composition. The hydration products in the CSA system contain a higher proportion of AFt phases. As SO_4^{2-} diffuse through the matrix, the AFt crystalline phases undergo transformation, leading to the formation of gypsum during the acid-etching process. This process consumes the hydration products and results in material structure deterioration. In the UHPC system, the incorporation

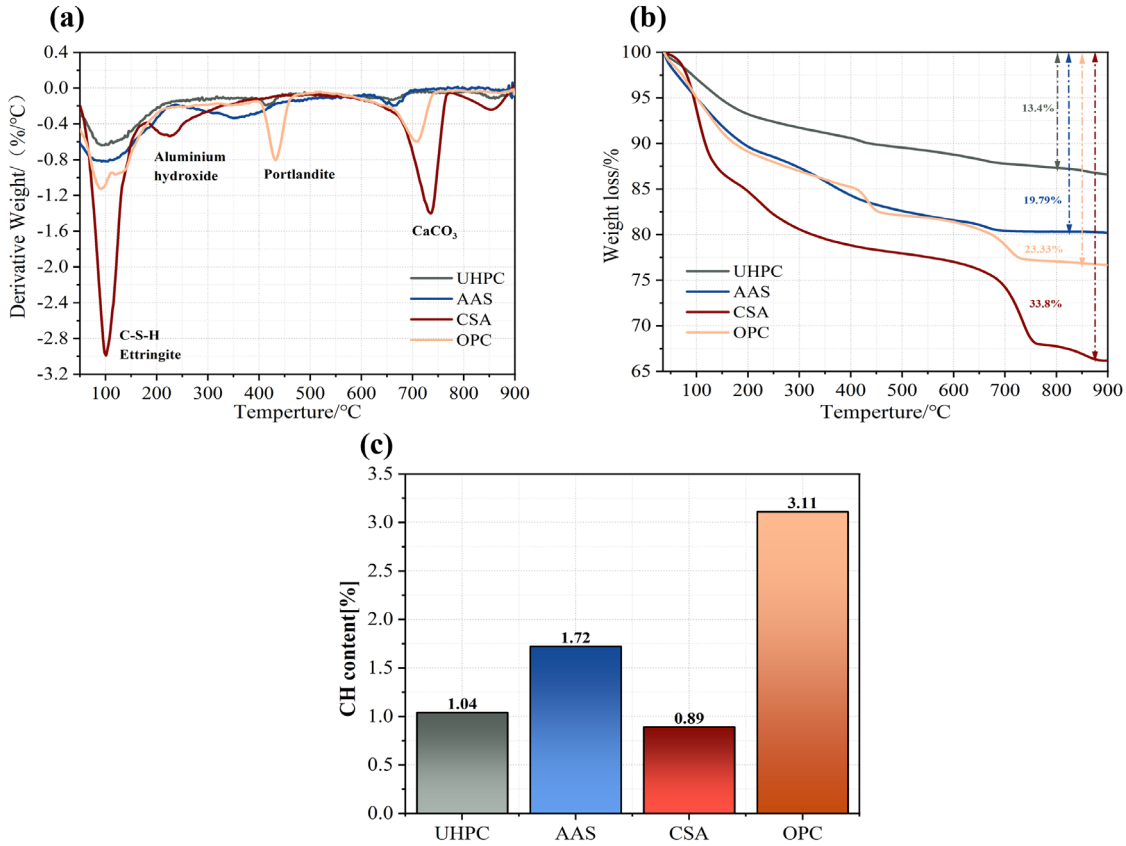

Figure 5 (a) DTG curves of the acid-etched layers in UHPC, AAS, CSA, and OPC samples; (b) corresponding thermogravimetric (TG) curves; (c) CH content (400–500°C)

of nanoparticles refined the matrix microstructure via pore-filling effects. This microstructural enhancement effectively restricted SO_4^{2-} diffusion within the composite, consequently decelerating the acid corrosion kinetics. In the AAS system, the alkaline activator provides sufficient alkaline ions to effectively neutralize the acidity of the solution, thereby slowing down the corrosion reaction. Thermogravimetric analysis revealed consistent weight loss characteristics in the OPC system across all temperature stages. The initial mass decrease, attributable to free water evaporation, was followed by more pronounced thermal decomposition events at elevated temperatures. The mass loss increases significantly with dehydration of hydration products such as C-S-H and Ca $(OH)_2$. At higher temperature intervals, the decomposition of calcium carbonate produces CaO and CO_2, which becomes the main factor in mass loss. As shown in Figure 5c, UHPC and CSA have the least CH content after 120 days sulfuric acid corrosion. This is because secondary hydration occurs between supplementary materials and CH, consuming CH to form gels. More gels make the structure denser, thus enhancing corrosion resistance. These findings elucidate the distinct acid corrosion resistance mechanisms among the investigated material systems (UHPC, AAS, CSA, and OPC), revealing fundamental structure-performance relationships under acidic conditions.

3.6 Infrared spectroscopy analysis

Fourier transform infrared spectroscopy (FTIR) was employed to characterize four mortar specimens following 120-day immersion in simulated acidic solutions. The FTIR spectra of each sample are presented in Figure 6. FTIR spectral analysis revealed a characteristic absorption band at approximately 978 cm^{-1} across all samples, indicating the formation of polymerized silicate network structures [65]. FTIR analysis identified characteristic $CaSO_4 \cdot 2H_2O$ vibrational peaks at 1125 cm^{-1} in all systems except AAS mortar, suggesting distinct sulfate phase evolution pathways among the material groups. Notably, the UHPC specimen exhibited attenuated $CaSO_4 \cdot 2H_2O$ vibrational peaks at ~1125 cm^{-1} in FTIR spectra. This observation correlates with UHPC's dense microstructure, which significantly impedes SO_4^{2-} diffusion and subsequent gypsum crystallization under acidic conditions. The dense microstructure of UHPC is significantly improved through the incorporation of reactive volcanic ash components, including SF and FA. These supplementary cementitious materials participate in secondary hydration reactions, thereby substantially increasing matrix densification [66]. In the CSA experimental group, the FTIR pattern exhibited characteristic vibrational peaks of calcite at 870 cm^{-1} and 610 cm^{-1}. The antisymmetric tensile vibration of SO_4^{2-} occurs at approximately 1120 cm^{-1}, and the bending vibration occurs at 610 cm^{-1}, as demonstrated by

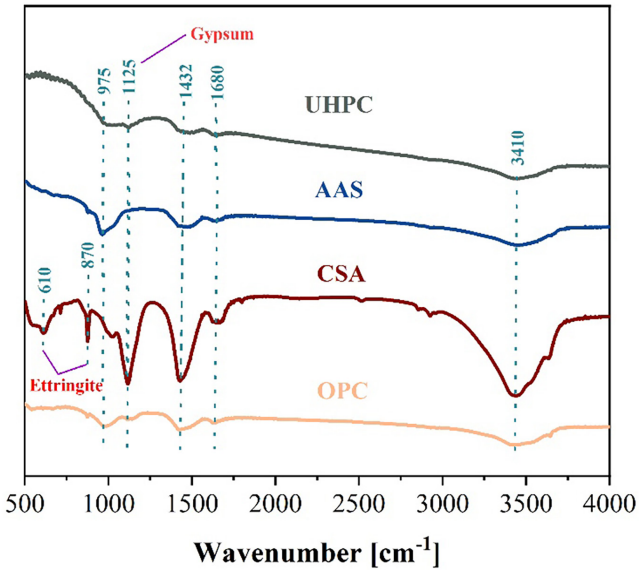

Figure 6 Infrared spectra of acid etching layer of UHPC, AAS, CSA and OPC samples

Chang et al. [67]. The vibrational peaks of the CSA system are more pronounced in these two bands. The smooth FTIR spectra of the UHPC samples suggest a homogeneous and stable composition, with characteristic peaks predominantly appearing in lower wavenumber regions, such as 975 cm^{-1} and 1125 cm^{-1}. These peaks are associated with the stretching vibrations of Si–O or Al–O bonds. The CSA system exhibits more intense vibrational peaks within these two spectral bands. The UHPC samples display smooth FTIR spectra, indicative of a uniform and chemically stable microstructure. Their characteristic peaks primarily occur at lower wavenumbers (e.g., 975 cm^{-1} and 1125 cm^{-1}), corresponding to Si–O and Al–O bond stretching vibrations. In addition, the characteristic vibrational peaks of carbonation products appeared at 1680 cm^{-1} and 1432 cm^{-1} in the FTIR profiles of the four collodion materials, which suggest secondary carbonation occurred of the materials during the acid etching process.

3.7 Mercury intrusion analysis

The influence of acid exposure on pore structure evolution in mortar specimens was revealed by Mercury Intrusion Porosimetry results, as illustrated in Figure 7. The results demonstrate that acid exposure alters the pore structure of all specimens; however, the response varies significantly among different materials in terms of pore size distribution and porosity evolution. As depicted in Figure 7a, the UHPC samples are predominantly characterized by the presence of minute pores with sizes less than 10 nm. This pore size distribution is in stark contrast to that observed in the AAS, CSA, and OPC samples, which exhibit a significantly higher proportion of larger pores. The measured total porosity values, as shown in Figure 7b, were 8.6% for UHPC, 23.86% for AAS, 34.13% for CSA, and 25.02% for OPC. These results demonstrate that the UHPC system exhibits significantly lower porosity compared to the other cementitious materials. The lower water-to-cement ratio, combined

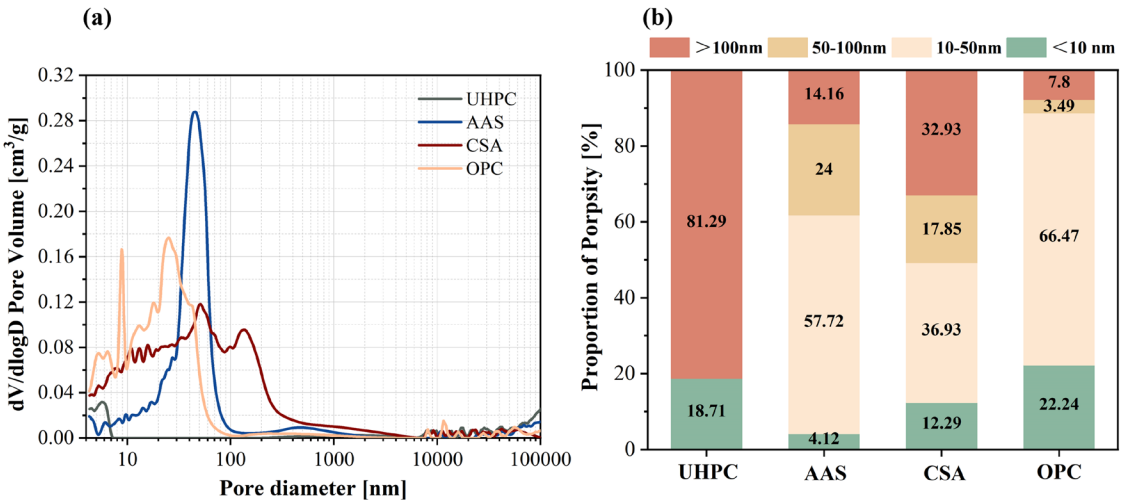

Figure 7 (a) Pore structure evolution of the acid-etched layers in UHPC, AAS, CSA, and OPC samples; (b) Pore structure distribution of the acid-etched layers in UHPC, AAS, CSA, and OPC samples

with the pozzolanic reaction facilitated by FA and SF, contributes to a more compact matrix structure. This structural compactness effectively inhibits the diffusion of SO_4^{2-} and enhances the material's durability in acidic environments [68]. In the CSA system, gypsum formation was partially suppressed owing to the limited availability of $Ca(OH)_2$. Nevertheless, hydration-derived calcite was predominantly located in the interfacial transition zone and aggregate periphery, where acicular calcite crystals contributed to pore structure refinement. The extended immersion period enhances SO_4^{2-} diffusion, catalyzing the conversion of gypsum to AFt. The associated volumetric expansion generates microcracks, thereby increasing the overall porosity of the system [59]. The AAS system develops a three-dimensional network gel structure through depolymerization and polycondensation reactions of silica-alumina rich glassy phases under high alkalinity. The significant heat release during this reaction induces chemical shrinkage, which may lead to microcrack formation within the pore structure [45]. During acid leaching, SO_4^{2-} migrates through microcracks, resulting in the dissolution of matrix hydration products and consequent deterioration of the pore structure. In the OPC system, acidic attack reacts with $Ca(OH)_2$ and C-S-H phases, generating soluble compounds and $CaSO_4$. This chemical transformation disrupts the original solid framework and induces secondary porosity. As the reaction proceeds, the fine pores coalesce or expand, resulting in an increase in pore size [45]. Furthermore, the continuous acidic attack produces gypsum, whose associated volumetric expansion induces internal stresses within the cementitious matrix. These stresses accelerate crack propagation and pore formation, ultimately compromising the mechanical performance and long-term durability of the cement-based materials.

3.8 Microscopic morphology

The acid-etched layers of four cementitious materials (UHPC, AAS, CSA, and OPC) exposed to a simulated acid environment for 120 days were analyzed by scanning electron microscopy (SEM) and energy-dispersive spectroscopy (EDS), as shown in Figures 8 and 9. A comparison of the microstructures and chemical compositions of these materials reveals variations in their durability when exposed to acidic solutions. UHPC exhibited optimal durability, as evidenced by low-magnification images showing that its matrix structure remained intact and dense. The high content of silicon (Si) and oxygen (O) elements

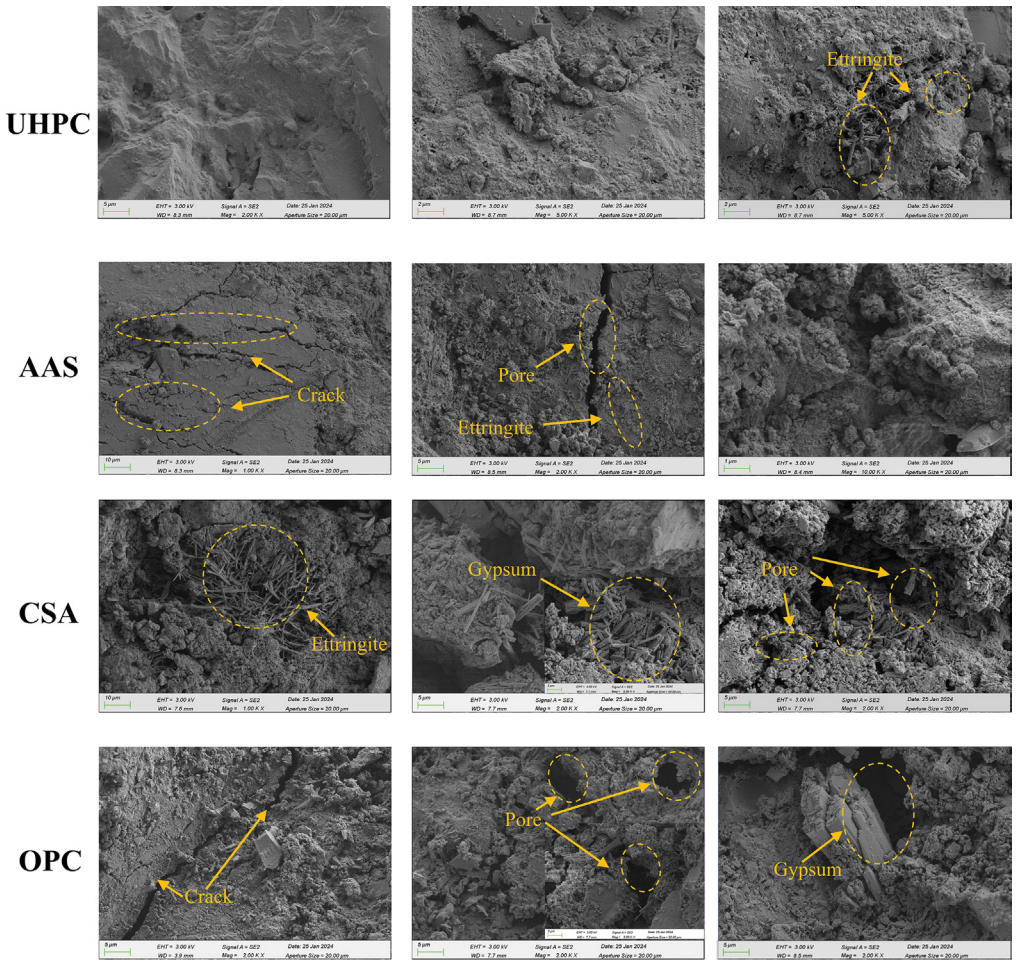

Figure 8 SEM of four cementitious materials under simulated acid erosion

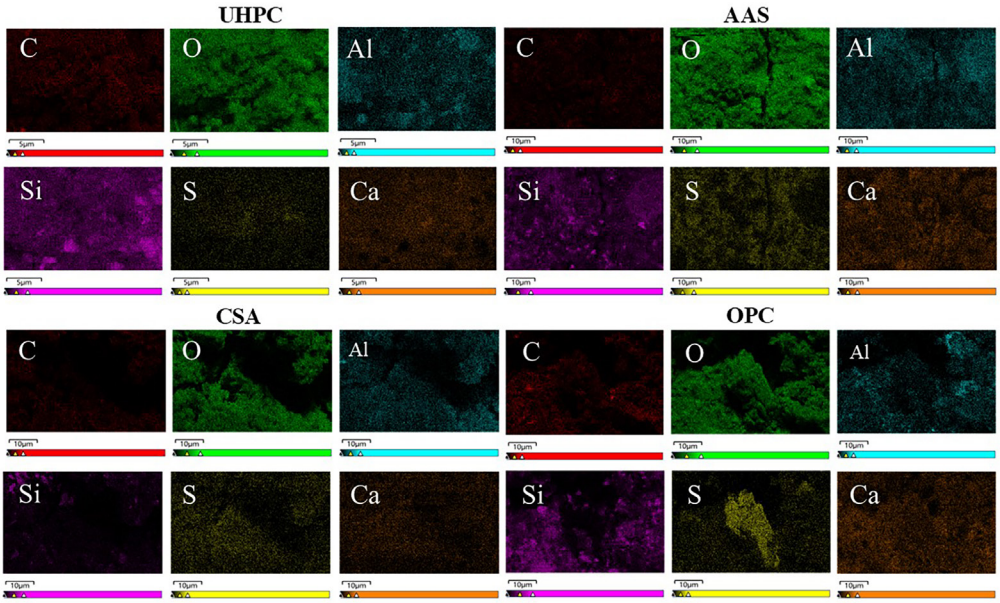

Figure 9 **EDS of four cementitious materials under simulated acid erosion**

correlates with the C–S–H gel generated by the pozzolanic reaction. This gel fills the pores and reduces the diffusion rate of SO_4^{2-}. Additionally, pin-rod-like calcite crystals were observed growing from the interior outward within the pores. They act as a pore-blocker, reducing the ingress of SO_4^{2-} ions and mitigating sulfate attack, and they help arrest microcracks, preventing their propagation. In contrast, AAS and CSA exhibited lower durability, with visible cracks and pores. Notably, CSA displayed more pronounced cracks and pores, indicating weaker corrosion resistance in acidic environments. In AAS, the formation and aggregation of the corrosion product ettringite (AFt) lead to matrix swelling and cracking. In CSA, the formation of numerous needle-and-rod-shaped calcium aluminate and gypsum crystals induces a volumetric expansion effect, which disrupts the matrix structure [59]. OPC exhibits the poorest durability, with severe damage to the matrix structure. This includes widespread cracking, a significant reduction in the cementing effectiveness of the hardened cement paste, and the formation of gypsum crystals, which further weakens the interface between the cementitious matrix and the aggregate. These factors collectively lead to substantial structural deterioration [69]. EDS analysis revealed that the corrosion products primarily contained calcium (Ca), sulfur (S), oxygen (O), aluminum (Al), and silicon (Si) elements, confirming the formation of gypsum crystals. In terms of elemental distribution, the high content of Si and O in UHPC enhances its durability [70]. In contrast, AAS and CSA exhibit significant enrichment of S around cracks, indicating that the acidic solution penetrates through microcracks and exacerbates the corrosion process [71]. The elemental distribution of Ca, S, O, Al, and Si in OPC further confirms the formation of gypsum crystals, which weakens the structural integrity of the material.

4 Conclusions

In the present work, the performance of UHPC, AAS, CSA, and OPC specimens was evaluated by replacing biological acids with simulated acids. The specimens were subjected to comprehensive analysis, including visual assessment, physical testing, mechanical property evaluation, and microstructural analysis. The corrosion mechanisms of these four cementitious materials under acid exposure were investigated, offering valuable insights for the long-term operation and maintenance of wastewater treatment facilities. The following are the primary conclusions:

(1) After 120 days of exposure to the simulated acid environment, the UHPC mortar still maintained a good appearance with no peeling in the edge areas and no visible cracking. In contrast, OPC mortar showed significant surface roughening, while AAS and CSA mortars showed significant cracks and holes after 120 days of immersion in the acid solution.
(2) After 120 days of exposure to the simulated acid environment, the appearance, mass loss, and erosion coefficient of the UHPC mortar specimens exhibited minimal deterioration and were superior to those of the other three cementitious materials. Specifically, the mass loss and erosion coefficient of UHPC mortar were controlled within 0.17% and 92.46%, respectively, which were 95.15% and 27.19% lower than those of OPC mortar.
(3) After 120 days under simulated acidic conditions, the four cementitious materials exhibited distinct degradation patterns and corrosion

mechanisms. UHPC showed the best sulfate resistance due to its dense microstructure and low pore volume. AAS and CSA cements, with moderate mesoporous structures, demonstrated good acid resistance. OPC had the poorest durability. AAS degraded via calcium aluminate hydrate decomposition, while CSA's corrosion was mainly determined by ettringite stability. UHPC's superior performance indicates its potential as a high-performance material for sewage disposal engineering.

Acknowledgement

The authors would like to acknowledge the National Key Research and Development Program of China (2025YFE0213000) and the Key Research and Development Program of Hubei Province (2024BAB108).

Funding Statement

The funding for this study is from the Key Research and Development Program of Hubei Province (2024BAB108).

Author Contributions

Jin Yang: Methodology, Writing—original draft, Supervision. Xudong Zhao: Investigation, Formal analysis, Writing—original draft. Xingyang He: Supervision, Review & editing. Gaoyuan Zhai: Investigation, Methodology. Ying Su: Validation, Conceptualization. Yingbin Wang: Methodology, Investigation. Yubo Li: Methodology, Investigation. Bohumír Strnadel: Conceptualization, Methodology. All authors reviewed and approved the final version of the manuscript.

Availability of Data and Materials

All data, models, and code generated or used during the study appear in the publishedarticle.

Ethics Approval

Not applicable.

Conflicts of Interest

The authors declare no conflicts of interest.

REFERENCES

[1] Krause MJ, Bronstein KE. Estimating national sludge generation and disposal from US drinking water and wastewater treatment plants. J Clean Prod. 2024;453(2):142121. doi:10.1016/j.jclepro.2024.142121.
[2] Allaire MC, Brusco B, Bakchan A, Elliott MA, Jordan MA, Maxcy-Brown J, et al. Water and wastewater infrastructure inequity in unincorporated communities. npj Clean Water. 2024;7(1):125. doi:10.1038/s41545-024-00409-3.
[3] Di Marcantonio C, Chiavola A, Spagnoli D, Meşe B, Margarita F, Gioia V, et al. Linking conventional activated sludge treatment plant performances for micropollutants removal to environmental risk and SimpleTreat model assessment. Int J Environ Sci Technol. 2024;21(11):7373–86. doi:10.1007/s13762-024-05476-0.
[4] Damion T, Chaunsali P. Biogenic acid resistance of calcium sulfoaluminate cement: revelations from a field study. Cem Concr Compos. 2024;145:105324. doi:10.1016/j.cemconcomp.2023.105324.
[5] Fytianos G, Tsikrikis A, Anagnostopoulos CA, Papastergiadis E, Samaras P. The inclusion of acidic and stormwater flows in concrete sewer corrosion mitigation studies. Water. 2021;13(3):261. doi:10.3390/w13030261.
[6] Chaudhari B, Panda B, Šavija B, Chandra Paul S. Microbiologically induced concrete corrosion: a concise review of assessment methods, effects, and corrosion-resistant coating materials. Materials. 2022;15(12):4279. doi:10.3390/ma15124279.
[7] Hong M, Niu D, Fu Q, Hui Z, Wan Z. Insights into bio-deterioration of concrete exposed to sewer environment: a case study. Constr Build Mater. 2024;412:134835. doi:10.1016/j.conbuildmat.2023.134835.
[8] Pereira Godinho J, de Medeiros MHF. Biogenic sulfur attack in a reinforced concrete sewage treatment plant. Re-Visited Mechanism Rehabilitation Proposal. Eng Fail Anal. 2021;124:105354. doi:10.1016/j.engfailanal.2021.105354.
[9] Shrestha K, Shrestha PP, Batista J. Evaluating life-cycle unit costs of traditional cement concrete and new polymer concrete manholes in wastewater systems. Buildings. 2024;14(9):2835. doi:10.3390/buildings14092835.
[10] Karunsena G, Gajanayake A, Udawatta N. Wastewater management in the construction sector: A systemic analysis of current practice in *Victoria*, Australia. Int J Constr Manag. 2024;24(11):1166–75. doi:10.1080/15623599.2022.2118102.
[11] Mueller EM, McAtee N, Azam HM. A review of biocorrosion issues and mitigation strategies in concrete sewers and wastewater collection systems. J Fail Anal Prev. 2026;6(6):3936. doi:10.1007/s11668-026-02393-x.
[12] Qi Z, Jia T, Cong W, Xi J. Mitigation of hydrogen sulfide production in sewer systems by inhibiting sulfate-reducing bacteria: a review. Front Environ Sci Eng. 2025;19(3):39. doi:10.1007/s11783-025-1959-x.
[13] Ding K, Zeng C. Study on the compressive strength, pore structure characteristics, and fractal dimension of the ecological porous concrete specimens based on ordinary Portland cement. Constr Build Mater. 2025;483:141795. doi:10.1016/j.conbuildmat.2025.141795.
[14] Zhang L, Qiu YY, Sharma KR, Shi T, Song Y, Sun J, et al. Hydrogen sulfide control in sewer systems: a critical review of recent progress. Water Res. 2023;240(4):120046. doi:10.1016/j.watres.2023.120046.
[15] Luimes RA, Rooyackers FAM, Suiker ASJ, Clemens FHLR, Bosco E. A novel approach for the lifetime prediction and structural health monitoring of concrete sewer systems exposed to biogenic sulphide corrosion. Cem Concr Res. 2024;181(6):107517. doi:10.1016/j.cemconres.2024.107517.
[16] Yuan Y, Zuo S, Zhang G, Fang H, Li S, Wang F. Understanding the early-stage spatially distributed behaviors of microbially induced concrete corrosion in the sewer system. Arch Civ Mech Eng. 2024;25(1):33. doi:10.1007/s43452-024-01091-5.
[17] Madraszewski S, Dehn F, Gerlach J, Stephan D. Experimentally driven evaluation methods of concrete sewers biodeterioration on laboratory-scale: a critical review. Constr Build Mater. 2022;320(7-9):126236. doi:10.1016/j.conbuildmat.2021.126236.
[18] Luimes RA, Scheperboer IC, Suiker ASJ, Bosco E, Clemens FHLR. Effect of biochemical attack on the mechanical performance of used concrete sewer pipes. Constr Build Mater. 2022;346(1):128390. doi:10.1016/j.conbuildmat.2022.128390.
[19] Jin L, Qiao L, Wu T, Zhou P, Xue P. Numerical analysis of sulfate accumulation and erosion behavior of concrete in sewage pipelines. Mech Time Depend Mater. 2026;30(1):8. doi:10.1007/s11043-026-09853-9.
[20] Xie M, Zhang X, Jing Y, Du X, Zhang Z, Tan C. Review on research and application of enhanced *in-situ* bioremediation agents for organic pollution remediation in groundwater. Water. 2024;16(3):456. doi:10.3390/w16030456.
[21] Canales C, Galarce C, Rubio F, Pineda F, Anguita J, Barros R, et al. Testing the test: a comparative study of marine microbial corrosion under laboratory and field conditions. ACS Omega. 2021;6(20):13496–507. doi:10.1021/acsomega.1c01762.
[22] Wells T, Melchers RE. An observation-based model for corrosion of concrete sewers under aggressive conditions. Cem Concr Res. 2014;61–62(19):1–10. doi:10.1016/j.cemconres.2014.03.013.
[23] Zhang W, Song Z. Experimental study of the product layer effect in the process of mortar under corrosion in sulfuric acid. Tehnički Vjesnik. 2024;31(1):98–103. doi:10.17559/tv-20230628000771.
[24] Multon S, Verdier J, Cagnon H, Nehme A, Sogbossi H. Numerical analysis of concrete permeability measurements in laboratory and in field. Cem Concr Res. 2024;178:107455. doi:10.1016/j.cemconres.2024.107455.
[25] Liu DE, Chen X, Feng Y, Rong H, Jia Y. Growth characteristics of sulfur oxidizing bacteria and their influence on concrete properties. Constr Build Mater. 2025;463(12):140105. doi:10.1016/j.conbuildmat.2025.140105.

[26] Iurchenko V, Melnikova O, Levashova Y, Kosenko N. Corrosion of concrete in a water management structure in conditions of biogenic sulfuric acid aggression. Key Eng Mater. 2023;953(4):55–62. doi:10.4028/p-0gbxtm.
[27] Qiao D, Matsushita T, Maenaka T, Shimamoto R. Long-term performance assessment of concrete exposed to acid attack and external sulfate attack. J Adv Concr Technol. 2021;19(7):796–810. doi:10.3151/jact.19.796.
[28] Zhang Y, Gu L, Zhang Q. Durability of manufactured sand concrete in atmospheric acidification environment. Case Stud Constr Mater. 2022;17(11): e01613. doi:10.1016/j.cscm.2022.e01613.
[29] Saha A, Tonmoy TM, Sobuz MHR, Aditto FS, Mansour W. Assessment of mechanical, durability and microstructural performance of sulphate-resisting cement concrete over Portland cement in the presence of salinity. Constr Build Mater. 2024;420(1):135527. doi:10.1016/j.conbuildmat.2024.135527.
[30] Ding L, Weiss WJ, Blatchley ER III. Effects of concrete composition on resistance to microbially induced corrosion. J Environ Eng. 2017;143(6): 04017014. doi:10.1061/(asce)ee.1943-7870.0001197.
[31] Bakera AT, Alexander MG. Sewer concrete subjected to biogenic acid corrosion: analysis of concrete deterioration phases using QEMSCAN. MATEC Web Conf. 2022;364:03012. doi:10.1051/matecconf/202236403012.
[32] Lee NK, Lee HK. Influence of the slag content on the chloride and sulfuric acid resistances of alkali-activated fly ash/slag paste. Cem Concr Compos. 2016;72(4):168–79. doi:10.1016/j.cemconcomp.2016.06.004.
[33] Zheng Z, Tan H, Zeng J, Yang J, Zheng G, Zhu M, et al. Ecological ultra-high performance concrete incorporating multi-scale and multi-source solid wastes as nano-micron filler, ultrafine binder and fine aggregate. Constr Build Mater. 2025;463:140002. doi:10.1016/j.conbuildmat.2025.140002.
[34] Yang J, Zhu M, He X, Su Y, Huang T, Wang X, et al. Converting iron mine tailings into composite aggregates for ultrahigh-performance mortar. J Mater Civ Eng. 2025;37(1):04024460. doi:10.1061/jmcee7.mteng-17779.
[35] Yang J, Zeng J, He X, Su Y, Tan H, Min H, et al. Utilization of submicron autoclaved aerated concrete waste to prepare eco-friendly ultra-high performance concrete by replacing silica fume. J Clean Prod. 2022;376:134252. doi:10.1016/j.jclepro.2022.134252.
[36] Yang J, Zeng J, He X, Hu H, Su Y, Bai H, et al. Eco-friendly UHPC prepared from high volume wet-grinded ultrafine GGBS slurry. Constr Build Mater. 2021;308(7):125057. doi:10.1016/j.conbuildmat.2021.125057.
[37] He F, Wang X, Zhang C, Hou Y, Liu Y. Coupled effects of different sulfuric acid concentrations and treatment methods on the corrosion rate of concrete materials. Case Stud Constr Mater. 2025;22(27):e04696. doi:10.1016/j.cscm.2025.e04696.
[38] Hu J, Li H, Guo X. Macro degradation resistance and microstructure evolution of ultra-high performance concrete in sewage environment. Constr Build Mater. 2026;509:145165. doi:10.1016/j.conbuildmat.2026.145165.
[39] Madraszewski S, Stephan D. The decisive role of the abrasion stress in concrete corrosion during acid attack–Comparison of resistance of different concrete types. Constr Build Mater. 2023;408(6):133736. doi:10.1016/j.conbuildmat.2023.133736.
[40] Liu Y, Tang Z, Tian H, Xu J, Zhang Z, Gu H, et al. Influence of further hydration on UHPC matrix properties. Mater Lett. 2024;377:137489. doi:10.1016/j.matlet.2024.137489.
[41] Nematzadeh M, Fallah-Valukolaee S. Erosion resistance of high-strength concrete containing forta-Ferro fibers against sulfuric acid attack with an optimum design. Constr Build Mater. 2017;154(4):675–86. doi:10.1016/j.conbuildmat.2017.07.180.
[42] Wang J, Kim YJ. Evolutionary characteristics of microstructural hydration and chloride diffusion in UHPC. Mater Des. 2023;225(7):111528. doi: 10.1016/j.matdes.2022.111528.
[43] Zhang Z, Scherer GW, Bauer A. Morphology of cementitious material during early hydration. Cem Concr Res. 2018;107(1511):85–100. doi:10.1016/j.cemconres.2018.02.004.
[44] Xi J, Liu J, Yang K, Zhang S, Han F, Sha J, et al. Role of silica fume on hydration and strength development of ultra-high performance concrete. Constr Build Mater. 2022;338(4):127600. doi:10.1016/j.conbuildmat.2022.127600.
[45] Zhao W, Fan Z, Li X, Kong L, Zhang L. Characterization and comparison of corrosion layer microstructure between cement mortar and alkali-activated fly ash/slag mortar exposed to sulfuric acid and acetic acid. Materials. 2022;15(4):1527. doi:10.3390/ma15041527.
[46] Teymouri M, Behfarnia K, Shabani A, Saadatian A. The effect of mixture proportion on the performance of alkali-activated slag concrete subjected to sulfuric acid attack. Materials. 2022;15(19):6754. doi:10.3390/ma15196754.
[47] Valencia-Saavedra WG, Mejía de Gutiérrez R, Puertas F. Performance of FA-based geopolymer concretes exposed to acetic and sulfuric acids. Constr Build Mater. 2020;257:119503. doi:10.1016/j.conbuildmat.2020.119503.
[48] Gu L, Bennett T, Visintin P. Sulphuric acid exposure of conventional concrete and alkali-activated concrete: assessment of test methodologies. Constr Build Mater. 2019;197(12):681–92. doi:10.1016/j.conbuildmat.2018.11.166.
[49] Dillard RJ, Murray CD, Deschenes RA. Belitic calcium sulfoaluminate cement subjected to sulfate attack and sulfuric acid. Constr Build Mater. 2022;343(6):128089. doi:10.1016/j.conbuildmat.2022.128089.
[50] Damion T, Cepuritis R, Chaunsali P. Sulfuric acid and citric acid attack of calcium sulfoaluminate-based binders. Cem Concr Compos. 2022;130: 104524. doi:10.1016/j.cemconcomp.2022.104524.
[51] Cao R, Yang J, Li G, Liu F, Niu M, Wang W. Resistance of the composite cementitious system of ordinary Portland/calcium sulfoaluminate cement to sulfuric acid attack. Constr Build Mater. 2022;329(17):127171. doi:10.1016/j.conbuildmat.2022.127171.
[52] Li X, Lin X, Lin K, Ji T. Study on the degradation mechanism of sulphoaluminate cement sea sand concrete eroded by biological sulfuric acid. Constr Build Mater. 2017;157(3):331–6. doi:10.1016/j.conbuildmat.2017.08.172.
[53] Bakharev T. Resistance of geopolymer materials to acid attack. Cem Concr Res. 2005;35(4):658–70. doi:10.1016/j.cemconres.2004.06.005.
[54] Albitar M, Mohamed Ali MS, Visintin P, Drechsler M. Durability evaluation of geopolymer and conventional concretes. Constr Build Mater. 2017;136(1):374–85. doi:10.1016/j.conbuildmat.2017.01.056.
[55] Mehta A, Siddique R. Sulfuric acid resistance of fly ash based geopolymer concrete. Constr Build Mater. 2017;146(325):136–43. doi:10.1016/j.conbuildmat.2017.04.077.
[56] Fares G, Abbas YM, Khan MI. Deterioration mechanisms of ultra-high-performance concrete under various sulfuric acid and sulfate attack conditions. Arab J Sci Eng. 2024;49(10):14429–45. doi:10.1007/s13369-024-09139-7.
[57] Kishore S, Arun Kumar A. Real-time monitoring and prediction of compressive strength of mortar and concrete. Mater Res Express. 2025;12(2): 025701. doi:10.1088/2053-1591/adb0a5.
[58] Liu J, Song G, Ge X, Liu B, Liu K, Tian Y, et al. Experimental study on the properties and hydration mechanism of gypsum-based composite cementitious materials. Buildings. 2024;14(2):314. doi:10.3390/buildings14020314.
[59] Xu C, Li Q, Wang P, Guo Y. Preparation and performance research of ecological concrete using waste wood. Case Stud Constr Mater. 2024;20(3): e03221. doi:10.1016/j.cscm.2024.e03221.
[60] Zhang W, Yao X, Yang T, Zhang Z. The degradation mechanisms of alkali-activated fly ash/slag blend cements exposed to sulphuric acid. Constr Build Mater. 2018;186:1177–87. doi:10.1016/j.conbuildmat.2018.08.050.
[61] Pang H, Qi W, Huang Y, Zhao Q, Zhang J, Zhao D, et al. Investigation of mechanical, microscopic, and leaching properties of coal-based solid waste geopolymer mortar activated by soda residue and phosphogypsum. Sci Total Environ. 2024;947:174459. doi:10.1016/j.scitotenv.2024.174459.
[62] Li J, Wu Z, Shi C, Yuan Q, Zhang Z. Durability of ultra-high performance concrete—A review. Constr Build Mater. 2020;255(8):119296. doi:10.1016/j.conbuildmat.2020.119296.
[63] Ma Q, Yang W, Duan Z, Liu H, Hua M, Deng Q. Influence of alkali-activators on acid rain resistance of geopolymer-recycled pervious concrete with optimal pore size. Materials. 2022;15(23):8368. doi:10.3390/ma15238368.
[64] Kong F, Xu F, Xiong Q, Xu S, Li X, Fu W, et al. Experimental research on properties of UHPC based on composite cementitious materials system. Coatings. 2022;12(8):1219. doi:10.3390/coatings12081219.
[65] Wang R, Zhang Y, Wu H, Jiang X. Study on the influencing factors of UHPC durability and its microscopic performance characterization. Materials. 2025;18(14):3268. doi:10.3390/ma18143268.
[66] Luan C, Wu Z, Han Z, Gao X, Zhou Z, Du P, et al. The effects of calcium content of fly ash on hydration and microstructure of ultra-high performance concrete (UHPC). J Clean Prod. 2023;415(3):137735. doi:10.1016/j.jclepro.2023.137735.
[67] Chang J, Gu Y, Ansari WS. Mechanism of blended steel slag mortar with CO_2 curing exposed to sulfate attack. Constr Build Mater. 2020;251(1): 118880. doi:10.1016/j.conbuildmat.2020.118880.
[68] Cheng H, Liu T, Zou D, Zhou A. Compressive strength assessment of sulfate-attacked concrete by using sulfate ions distributions. Constr Build Mater. 2021;293(8):123550. doi:10.1016/j.conbuildmat.2021.123550.
[69] Wang Y, Zhang S, Niu D, Fu Q. Quantitative evaluation of the characteristics of air voids and their relationship with the permeability and salt freeze–thaw resistance of hybrid steel-polypropylene fiber-reinforced concrete composites. Cem Concr Compos. 2022;125(7):104292. doi:10.1016/j.cemconcomp.2021.104292.
[70] Mei J, Yuan C, Niu Y, Zhang J, Li S, Li H. Sulfate resistance of alkali-activated slag/metakaolin/fly ash cementitious materials. ZKG Int. 2024;77(1): 50–9. doi:10.32604/zkg.2024.01.02.
[71] Mei J, Yin C, Zhao Y, Niu Y, Xie A, Li S. Effect of calcium carbide slag on the durability of alkali-activated ground granulated blast furnace slag-fly ash cementitious system. ZKG Int. 2024;77(8):42–50. doi:10.32604/zkg.2024.08.01.